ChemComm
Chemical Communications

Accepted Manuscript

This article can be cited before page numbers have been issued, to do this please use: N. Patil, H. McKeever, M. Ahlawat, K. M. Ryan and S. Singh, *Chem. Commun.*, 2026, DOI: 10.1039/D6CC01363E.

ROYAL SOCIETY OF CHEMISTRY

rsc.li/chemcomm

ChemComm

View Article Online
DOI: 10.1039/D6CC01363E

COMMUNICATION

Template-Guided Sodium Intercalation Enables Phase-Pure Alkali Metal-based Ternary Chalcogenides Nanocrystals

Received 00th January 20xx,
Accepted 00th January 20xx

DOI: 10.1039/x0xx00000x

Niraj Nitish Patil*[a], Hannah McKeever[a], Monika Ahlawat[a], Kevin M Ryan[a], Shalini Singh*[a]

[a] Department of Chemical Sciences and Bernal Institute, University of Limerick, V94 T9PX Limerick, Ireland

Alkali metal–based ternary chalcogenides are promising materials which remain synthetically underexplored. Here, a template-based strategy enables synthesis of colloidal $NaInS_2$ and $NaIn_3Se_5$ nanocrystals. Mechanistic insights reveal sodium intercalation as a predictive route to phase-pure ABZ nanocrystals.

Chalcogenide materials have attracted considerable attention owing to their diverse applications in energy storage and conversion.[1, 2] Within this broad class, alkali metal-based ternary chalcogenides, commonly referred to as ABZ materials, where A = alkali metal, B = transition metal, Z = chalcogen, are promising emerging candidates for functional energy materials.[3-9] Their diverse crystal structures, tunable functionalities and ability to be engineered as inorganic semiconductors make them attractive for a wide range of applications.[10-15] Despite their promise, the synthesis of ABZ nanomaterials (NMs) remains a central challenge. Traditional synthetic protocols rely on a trial-and-error approach, guided by factors such as precursor reactivities, molar ratios, decomposition temperatures, and growth times to achieve phase-pure products. While effective in many cases, this strategy is time-consuming and constrained by the disparate chemical reactivities and kinetics across different elemental combinations.[5] Synthetic protocols developed for one ABZ composition cannot be directly applied to others, largely because predicting atomic arrangements during crystal formation is inherently difficult. Overcoming this challenge is essential to enable rational design and accelerate the synthesis and discovery of new, functionally relevant NMs.

Colloidal chemistry offers a powerful platform for probing reaction kinetics, elucidating mechanisms and tracking intermediate formation, thereby paving the way toward a predictive synthetic framework.[16-22] A promising route toward generalising ABZ nanostructures synthesis is the template approach, in which a binary metal-chalcogenide nanocrystal (NC) or first-generation (G-1) synthon, undergoes partial cation exchange (CE). Here, an additional cation is incorporated in situ into the host lattice, enabling the rational construction of a multicomponent structure.[23] While highly promising, this approach has so far been restricted mainly to Cu-chalcogenides,[16] highlighting the need for further exploration to establish a general framework applicable across the broader ABZ material class.

Herein, we report a template-based colloidal synthesis approach for In-based ABZ nanostructures. We demonstrate the first nanoscale synthesis of $NaIn_3Se_5$ and extend the strategy to $NaInS_2$ NCs. We establish the synthetic approach by providing comprehensive mechanistic insights for both systems using X-ray diffraction (XRD), transmission electron microscopy (TEM), and X-ray photoelectron spectroscopy (XPS), and further evaluate their optical properties for potential optoelectronic applications. The combination of precise synthetic control and mechanistic understanding provides a predictive pathway for NC formation in ABZ systems, representing a significant step toward the rational design of functional NMs.

$NaIn_3Se_5$ NCs were prepared using a colloidal hot injection synthesis (see experimental section for detailed synthesis). XRD analysis confirmed that the NCs is in the trigonal P (32) space group (Figure 1a and S1). The experimental peak positions and intensities agree with the $NaIn_3Se_5$ reference pattern (PDF No. 01-071-3539). Rietveld refinement of the experimental pattern yielded cell parameters a = 24.582 Å, b = 24.582 Å, and c = 17.427 Å (Figure S2). The refinement shows excellent agreement between the experimental data and the reference pattern, with low values of the goodness-of-fit (~1.14) and the weighted profile residual (R_{wp}) (~7.84), confirming the phase purity. The corresponding crystal structure (Figure S1b) reveals a complex 3D framework composed of superpolydedral chalcogenide clusters.[24] TEM images reveal a hexagonal nanocuboid like morphology for $NaIn_3Se_5$ NCs (Figure 1b).

[a] Department of Chemical Sciences and Bernal Institute, University of Limerick, V94 T9PX Limerick, Ireland
Corresponding Author: Shalini.Singh@ul.ie Niraj.Patil@ul.ie

View Article Online
DOI: 10.1039/D6CC01367F

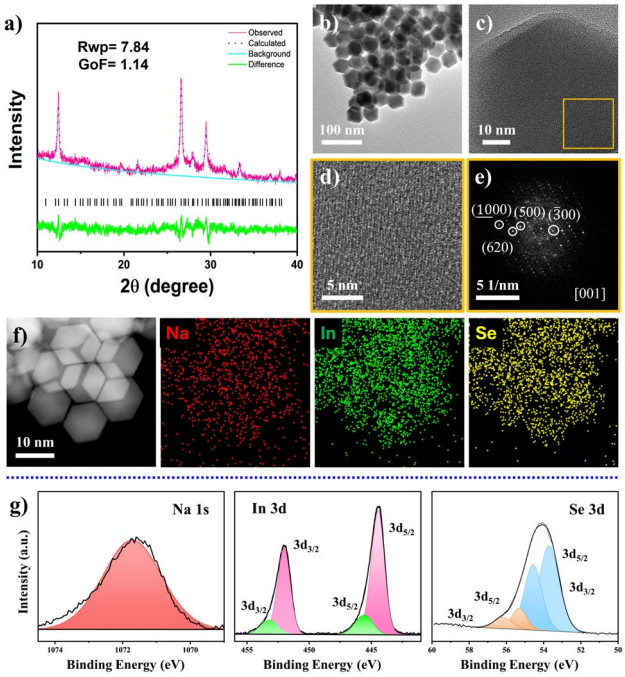

Figure 1. Structural and compositional analysis of $NaIn_3Se_5$ NCs (a) XRD analysis using Rietveld refinement, reference pattern PDF No. 01-071-3539 (b) TEM image of $NaIn_3Se_5$ NCs (c-e) High resolution TEM image of $NaIn_3Se_5$ NCs with corresponding FFT pattern (f) HAADF image and corresponding STEM-EDS maps for Na, In and Se and (g) high resolution XPS spectra of Na, In and Se.

High-resolution TEM (HRTEM) combined with fast Fourier transform (FFT) analysis (Figures 1c-e) further confirms the formation of the hexagonal crystal structure. The FFT patterns display d-spacings of ~7.09 Å, 4.26 Å, and 2.95 Å, corresponding to the $(\bar{3}00)$, (500), and (620) planes, respectively. Element maps obtained from scanning transmission electron microscopy with energy dispersive spectroscopy (STEM-EDS) confirmed the simultaneous presence and uniform distribution of Na, In, and Se in the NC (Figure 1f). XPS was performed to confirm the chemical composition and oxidation states of the NCs (Figure 1g, S3). The high-resolution XPS spectra (Figure 1g) confirm the presence of Na, In and Se as the primary elements of NCs. The Na 1s spectrum (Figure 1g) shows a peak at ~1071.7 eV, characteristic of the Na^+ species. In the In 3d spectra (Figure 1g), peak fitting reveals a doublet at 444.3 eV and 452.0 eV corresponding to the In $3d_{5/2}$ and $3d_{3/2}$ orbitals in the +3-oxidation state arising from structure. A higher energy doublet at 446.6 eV and 454.5 eV is attributed to oxidised In species.[25] The high-resolution Se 3d spectrum (Figure 1g) displays two distinct doublets. The first, located at 53.7 eV and 54.6 eV, is assigned to selenide species, while the second doublet at 55.3 eV and 56.2 eV corresponds to surface-oxidised selenium.

The XPS survey spectra (Figure S3) additionally reveal the presence of C and N, which originate from the surface-bound oleylamine (OLA) ligand. The presence of OLA was further verified by the Fourier transform infrared spectroscopy (FTIR) (Figure S4), which exhibits characteristic vibrational modes at ~1130 cm^{-1} (C–N stretching), 1600 cm^{-1} (N–H bending), and a broad band at ~3350 cm^{-1} corresponding to the NH_2 stretching vibrations.[26] The Raman spectrum of $NaIn_3Se_5$ exhibits two prominent vibrational modes at 160 and 234 cm^{-1}, which are associated with the covalently bonded In–Se framework (Figure S5). The intense peak at 160 cm^{-1} can be assigned to the primary optical A_1 symmetric breathing mode of the [$InSe_4$] tetrahedra, like related indium-selenium ordered-vacancy compounds.[27] The peak at 234 cm^{-1} corresponds to higher-frequency asymmetric stretching vibrations of In–Se bonds.

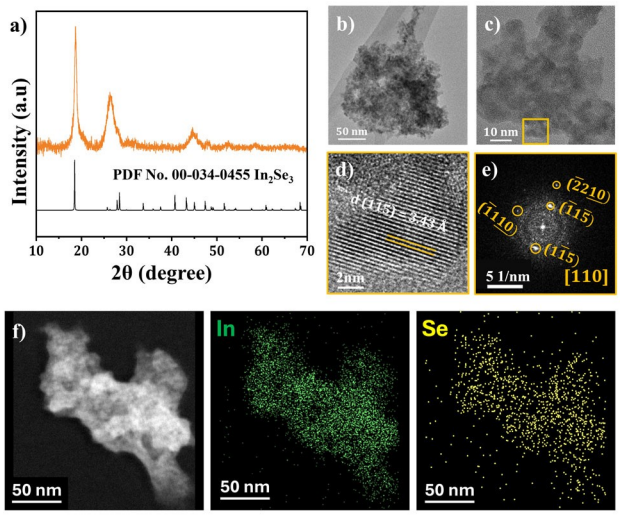

Figure 2. Analysis of In_2Se_3 template formed in situ before Na injection (a) XRD analysis (b) TEM image of In_2Se_3 nanoparticles (c) HRTEM image of In_2Se_3 nanoparticles (d-e) enlarged view of the highlighted area (orange square) in (c) and its FFT showing crystallographic orientation and interplanar distances. (f) HAADF image, and corresponding STEM-EDS maps for In and Se.

To elucidate the template formation and reaction pathway leading to $NaIn_3Se_5$ NCs, an aliquot was extracted from the reaction mixture at 260 °C prior to the incorporation of Na precursor in the flask. The structural and morphological evolution of this intermediate was analysed by XRD and TEM (Figure 2). XRD analysis (Figure 2a) confirms that the intermediate crystallises as In_2Se_3 in the trigonal $R\bar{3}m$ space group. The broad diffraction features indicate a low degree of long-range order, consistent with the formation of very small NCs. The TEM images (Figure 2b, c) corroborate the presence of small In_2Se_3 NCs. HRTEM (Figure 2c), combined with corresponding FFT analysis (Figure 2d, e), further confirms the trigonal crystal structure. The FFT pattern displays d-spacings of ~3.43 Å which can be indexed to the $(1\bar{1}5)$ plane in close agreement with the reference In_2Se_3 structure (PDF: 01-085-9716). And EDS analysis further confirmed the formation of binary In_2Se_3 template (Figure 2f).

The *in-situ* formation of this In_2Se_3 phase is a critical prerequisite for the subsequent synthesis of $NaIn_3Se_5$, underscoring its role as a structural template. In this template-mediated growth mechanism, the pre-formed indium selenide lattice undergoes atomic reorganisation upon hot injection of the Na precursor, driving a symmetry reduction from trigonal $\bar{R}3m$ to trigonal P(32) and yielding $NaIn_3Se_5$. Control experiments were conducted to determine the optimal

temperature window for $NaIn_3Se_5$ formation (Figure S6). The phase evolution of Na–In–Se NCs was first examined by XRD as a function of Na-oleate injection temperature. At 220 °C, the XRD pattern exhibits broad and weak spectra, indicating low crystallinity and incomplete conversion of the binary In–Se template into the ternary Na–In–Se compound (Figure S6). This is supported by TEM analysis, which shows predominantly small, irregular nanoparticles (NPs) along with hexagonal nanoplate-like crystallites, suggesting heterogeneous growth and incomplete phase transformation (Figure S7a-e). In contrast, at 300 °C, additional diffraction peaks, indicating the coexistence of $NaIn_3Se_5$ and $NaInSe_2$ ternary phases (Figure S6). TEM images of this sample reveal two distinct morphologies, NPs and plate-like crystals, further supporting the formation of two crystalline Na–In–Se phases at higher injection temperature (Figure S7f-i). Overall, these results demonstrate that the Na-oleate injection temperature strongly governs both phase selectivity and morphology, with lower temperature favouring residual binary In–Se, while higher temperature promotes competing ternary Na–In–Se phases. Additionally, to understand the role of the Se precursor and assess the versatility of the synthesis, elemental Se powder was replaced with diphenyldiselenide (DPDSe) and selenourea. XRD analysis confirms the formation of $NaIn_3Se_5$ phase in both cases (Figure S8). The DPDSe-derived sample shows sharper and more defined peaks, indicating better crystallinity, whereas the selenourea-derived sample exhibits broad and weak peaks, suggesting smaller crystallites and increased structural disorder. TEM analysis further reveals precursor-dependent morphology. DPDSe produces well-defined, faceted NPs with clear lattice fringes and distinct spots in FFT, confirming good crystallinity (Figure S9a-d). In contrast, selenourea leads to highly aggregated, smaller particles, indicating rapid nucleation and less controlled growth (Figure S9e-h). Overall, the Se precursor strongly influences both the crystallinity and morphology of $NaIn_3Se_5$.

To evaluate the generality of the template-mediated synthesis strategy across the ABZ compositional space, we investigated anion substitution at the Z site by replacing selenium with sulfur to access a sulfide-based ternary phase. For this case, of elemental selenium was directly substituted with an amount of elemental sulfur; all other conditions for the synthesis were maintained identical to those for the $NaIn_3Se_5$ NCs synthesis. This controlled substitution enabled us to assess whether template-driven atomic reorganisation can accommodate changes in anion chemistry and local lattice metrics without disrupting the overall crystallographic framework.

Similarly to the trigonal $NaIn_3Se_5$ NCs, phase-pure $NaInS_2$ NCs were obtained after a 60-minute reaction time, indicating that the template-based growth mechanism is robust to chalcogen substitution. Structural characterisation by XRD analysis revealed that the $NaInS_2$ adopts the same trigonal P(32) space group as $NaIn_3Se_5$, suggesting that the underlying framework topology is preserved despite the reduced ionic radius and increased electronegativity of sulfur (Figure 3a & S10). Rietveld refinement confirms the phase purity of the NCs, yielding a GOF value of 1.05 and a Rwp of 9.24 with refined cell parameters in close agreement with the reference pattern (Figure 3a & S11). The crystal structure consists of a 3D network of corner- and edge-sharing NaS_6 and InS_6 octahedra with average Na–S and In–S bond lengths of 2.88 Å and 2.65 Å, respectively, as shown in Figure S10b.[28] The hexagonal morphology of the NCs is displayed in Figure 3b,c while HRTEM images (Figure 3d-e) further confirm the formation of $NaInS_2$ NCs through the measured d-spacings (~5.21 Å) with the reference values for both the (110) and (2$\bar{1}$0) planes. Elemental mapping by STEM-EDS (Figure 3f) confirmed the uniform distribution of Na, In and S within the NCs.

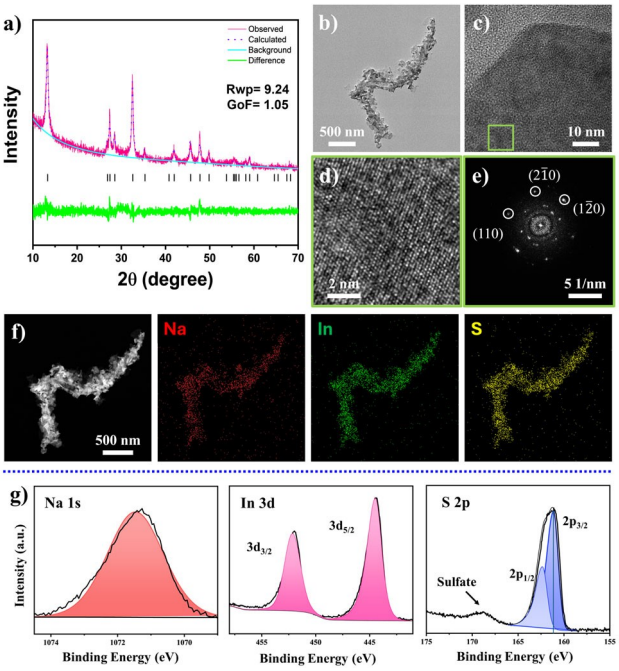

Figure 3. Structural and compositional analysis of $NaInS_2$ NCs (a) XRD analysis using Rietveld refinement, reference pattern PDF No. 04-003-9955 (b) TEM image of $NaInS_2$ NCs (c-e) High resolution TEM image of $NaInS_2$ NCs with corresponding fast Fourier transform (FFT) pattern (f) HAADF image and corresponding STEM-EDS maps for Na, In and S and (g) high resolution XPS spectra of Na, In and S.

To further verify the composition, XPS analysis was performed on $NaInS_2$ NCs. The survey spectra confirmed the presence of Na, In, and S as the primary elements (Figure S3), which displayed a peak at 444.5 eV, characteristic of the In $3d_{5/2}$ orbital in the +3-oxidation state (Figure 3g). The S 2p spectrum (Figure 3g) exhibited doublet at 161.2 eV, consistent with sulfide (S^{2-}), and broad peak at 168.7 eV, attributed to surface oxidation forming the sulfate species (SO_4^{2-}). The surface functionalities of the synthesised NCs were found to be identical to those of $NaIn_3Se_5$, with OLA acting as a surface-bound ligand (Figure S12). Raman spectra exhibited characteristic peaks at 160 and 291 cm^{-1}, which are consistent with previous reports, further confirming the formation of $NaInS_2$ phase (Figure S13).[29] Further mechanistic insight was provided by an aliquot study in which the aliquot was extracted prior to Na incorporation during $NaInS_2$ synthesis (Figure S14), revealing the formation of $In_{1.95}S_3$ as an intermediate phase. This sulfide template reflects

on the role of indium selenide in the selenide system and facilitates the subsequent incorporation of Na through atomic rearrangement within the pre-organised indium sulfide lattice, ultimately yielding phase-pure $NaInS_2$. Indium sulphide served as a template, facilitating the growth of phase-pure $NaInS_2$. In analogy to $NaIn_3Se_5$, systematic variations in reaction temperature, reaction time, and sulfur precursor were performed for $NaInS_2$ to demonstrate the tunability and general applicability of the synthetic strategy (detailed info in SI section S2.11). This observation of indium chalcogenide templates across both Se and S validates that ABZ NCs form via an *in-situ* developed template-based approach rather than direct ternary nucleation.

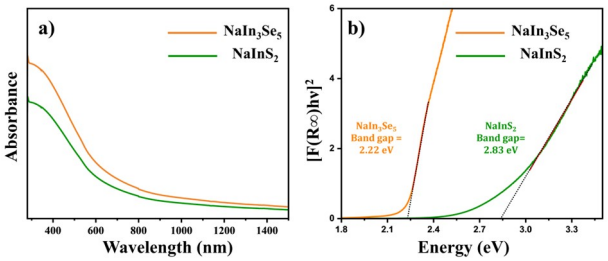

Figure 4: Optical property analysis a) Absorbance spectrum b) Tauc plot analysis for for $NaIn_3Se_5$ and $NaInS_2$ NCs

Finally, we studied the optical behaviour of $NaIn_3Se_5$ NCs and $NaInS_2$ NCs using UV-Vis-NIR absorption and diffuse reflectance spectroscopy. Both NCs show strong absorption in the UV-vis region with absorption onset around the NIR region, as shown in Figure 4a. The optical band gaps were estimated using Tauc plots derived from reflectance spectra of $NaIn_3Se_5$ NCs and $NaInS_2$ NCs. The experimentally measured band gaps of 2.22 eV and 2.83 eV for $NaInS_2$ NCs and $NaIn_3Se_5$ NCs, respectively (Figure 4b), are consistent with the previous computational reports.[30-33] With these optimal band gaps and significant absorption characteristics, $NaIn_3Se_5$ and $NaInS_2$ NCs can be promising materials for photocatalysis, tandem solar cell absorbers, and photodetectors.[24]

In summary, we have overcome a critical challenge in the synthesis of ternary alkali metal chalcogenides by developing a facile template-based strategy. This approach relies on a metal chalcogenide synthon to effectively direct phase evolution and guide the formation of the desired nanocrystalline $NaIn_3Se_5$ structure. The versatility of the method was further demonstrated in the sulfide system, underscoring its broader applicability. We also display the relationship between the binary synthon and the resulting ternary crystal phase. The successful extension from selenide to sulfide systems demonstrates the generalizability of this synthetic strategy, suggesting its potential applicability to other systems containing different alkali metals such as Li or K, or alternative metal centers such as Ga through suitable selection of metal and chalcogen precursors. Extending this strategy to other alkali metals may enable streamlined discovery and provide new opportunities for the targeted design of functional ABZ NMs for energy applications.

Conflicts of interest

View Article Online
DOI: 10.1039/D6CC01363E

"There are no conflicts to declare".

Data availability

The data that support the findings of this study are available on request from the corresponding author.

Supplementary information includes material and method for synthesis of nanostructures with extra data regarding: (i) XRD analysis, (ii) Refinement Parameters for Se and S systems (iii) STEM-EDS data (iv) XPS spectra (v) control experiments (vi) XRD, TEM and STEM EDS for aliquots.

Acknowledgment

This publication has emanated from research conducted with the financial support of Taighde Éireann – Research Ireland under Grant number 22/FFP-P/11591. H.M. acknowledges funding from the Research Ireland centre MaREI. M.A. acknowledges funding from Research Ireland fellowship GOIPD/2025/1538.

References:Uncategorized References

1. C. Q. Li and J. J. Wang, Small, 2024, 20, 2404798.
2. Y. Zhang, Y. Huang, S. S. Zhu, Y. Y. Liu, X. Zhang, J. J. Wang and A. Braun, Small, 2021, 17, 2100320.
3. N. N. Patil, R. Wu, C. Fiedler, N. Kapuria, B. Nan, N. Jakhar, A. Cabot, M. Ibáñez, K. M. Ryan, A. M. Ganose and S. Singh, ACS Energy Letters, 2026, 11, 481–488.
4. H. McKeever, N. Kapuria, A. Nicolson, S. Sen, D. Scanlon, K. M. Ryan and S. Singh, Nano Letters, 2025, 25, 4652–4658.
5. H. McKeever, N. N. Patil, M. Palabathuni and S. Singh, Chemistry of Materials, 2023, 35, 9833–9846.
6. N. Kapuria, B. Nan, T. E. Adegoke, U. Bangert, A. Cabot, S. Singh and K. M. Ryan, Chemistry of Materials, 2023, 35, 4810–4820.
7. A. M. Medina-Gonzalez, P. Yox, Y. Chen, M. A. S. Adamson, B. A. Rosales, M. Svay, E. A. Smith, R. D. Schaller, K. Wu, A. J. Rossini, K. Kovnir and J. Vela, Chemistry of Materials, 2022, 34, 7357–7368.
8. Y.-T. Huang, S. R. Kavanagh, D. O. Scanlon, A. Walsh and R. L. Z. Hoye, Nanotechnology, 2021, 32, 132004–132004.
9. Z. Sun, N. Pham, S. Derakhshan and R. L. Brutchey, Chemical Science, 2025, 16, 18722–18728.
10. M. Bouchenafa, Y. Bourourou, A. Khelefhoum, H. Boulebda, M. A. Fadla, A. Benmakhlouf, S. Maabed, M. Halit and M. Sidoumou, Computational Condensed Matter, 2022, 30, 00644.
11. A. Banerjee, K. H. Park, J. W. Heo, Y. J. Nam, C. K. Moon, S. M. Oh, S. T. Hong and Y. S. Jung, Angewandte Chemie, 2016, 128, 9786–9790.
12. N. Ma, Y.-Y. Li, L. Chen and L.-M. Wu, Journal of the American Chemical Society, 2020, 142, 5293–5303.
13. Y. Chen, Y. Shen, X. Li, J. Sun and Q. Wang, Advanced Theory and Simulations, 2020, 3, 2000169.
14. Z. Xia, H. Fang, X. Zhang, M. S. Molokeev, R. Gautier, Q. Yan, S.-H. Wei and K. R. Poeppelmeier, Chemistry of Materials, 2018, 30, 1121–1126.
15. M. M. Hossain, M. A. Ali, M. M. Uddin, M. A. Hossain, M. Rasadujjaman, S. H. Naqib, M. Nagao, S. Watauchi and I.

View Article Online
DOI: 10.1039/D6CC01363E

Tanaka, Materials Today Communications, 2021, 26, 101988–101988.
16. N. Kapuria, N. N. Patil, K. M. Ryan and S. Singh, Nanoscale, 2022, 14, 2885–2914.
17. N. Kapuria, N. N. Patil, A. Sankaran, F. Laffir, H. Geaney, E. Magner, M. Scanlon, K. M. Ryan and S. Singh, Journal of Materials Chemistry A, 2023, 11, 11341–11353.
18. M. Mishra, N. N. Patil, M. Zubair, N. Kapuria, V. Lebedev, T. E. Adegoke, K. M. Ryan and S. Singh, Nanotechnology, 2022, 33, 305602–305602.
19. N. N. Patil, A. Sankaran, T. E. Adegoke, K. M. Ryan and S. Singh, Small Structures, 2025, 6, 2500159.
20. S. Sen, N. N. Patil, A. Bora, M. Palabathuni, T. E. Adegoke, K. M. Ryan, K. Rossi and S. Singh, Nano Letters, 2025, 25, 12207–12215.
21. A. Loiudice and R. Buonsanti, Nature Synthesis, 2022, 1, 344–351.
22. M. Ibáñez, S. C. Boehme, R. Buonsanti, J. De Roo, D. J. Milliron, S. Ithurria, A. L. Rogach, A. Cabot, M. Yarema, B. M. Cossairt, P. Reiss, D. V. Talapin, L. Protesescu, Z. Hens, I. Infante, M. I. Bodnarchuk, X. Ye, Y. Wang, H. Zhang, E. Lhuillier, V. I. Klimov, H. Utzat, G. Rainò, C. R. Kagan, M. Cargnello, J. S. Son and M. V. Kovalenko, ACS Nano, 2025, 19, 31969–32051.
23. Q. A. Akkerman, A. Genovese, C. George, M. Prato, I. Moreels, A. Casu, S. Marras, A. Curcio, A. Scarpellini, T. Pellegrino, L. Manna and V. Lesnyak, ACS Nano, 2015, 9, 521–531.
24. S.-F. Li, X.-M. Jiang, B.-W. Liu, D. Yan, C.-S. Lin, H.-Y. Zeng and G.-C. Guo, Chemistry of Materials, 2017, 29, 1796–1804.
25. S.-W. Hsiao, C.-S. Yang, H.-N. Yang, C.-H. Wu, S.-K. Wu, L.-Y. Chang, Y.-T. Ho, S.-J. Chang and W.-C. Chou, Frontiers in Materials, 2022, 9, 871003.
26. A. N. Roth, Y. Chen, M. A. S. Adamson, E. Gi, M. Wagner, A. J. Rossini and J. Vela, ACS Nano, 2022, 16, 12024–12035.
27. R. Vilaplana, S. G. Parra, A. Jorge-Montero, P. Rodríguez-Hernández, A. Munoz, D. Errandonea, A. Segura and F. J. Manjón, Inorganic Chemistry, 2018, 57, 8241–8252.
28. A. Jain, S. P. Ong, G. Hautier, W. Chen, W. D. Richards, S. Dacek, S. Cholia, D. Gunter, D. Skinner, G. Ceder and K. A. Persson, APL Materials, 2013, 1, 011002.
29. J. K. Larsen, K. V. Sopiha, C. Persson, C. Platzer-Bjorkman and M. Edoff, Adv Sci (Weinh), 2022, 9, 2200848.
30. M. M. Hossain, M. A. Hossain, S. A. Moon, M. A. Ali, M. M. Uddin, S. H. Naqib, A. K. M. A. Islam, M. Nagao, S. Watauchi and I. Tanaka, Journal of Materials Science: Materials in Electronics, 2021, 32, 3878–3893.
31. Y. Fu, X. Duan, M. Xing, N. Zhang, X. Luo, H. Wang and Y. Ma, Materials Letters, 2014, 124, 141–143.
32. A. Kudo, A. Nagane, I. Tsuji and H. Kato, Chemistry Letters, 2002, 31, 882–883.
33. N. Takahashi, H. Ito, A. Miura, N. C. Rosero-Navarro, Y. Goto, Y. Mizuguchi, C. Moriyoshi, Y. Kuroiwa, M. Nagao, S. Watauchi, I. Tanaka and K. Tadanaga, Journal of Alloys and Compounds, 2018, 750, 409–413.

View Article Online
DOI: 10.1039/D6CC01363E

Data Availability Statement

The data that support the findings of this study are available on request from the corresponding author.

Supplementary information includes material and method for synthesis of nanostructures with extra data regarding: (i) XRD analysis, (ii) Refinement Parameters for Se and S systems (iii) STEM-EDS data (iv) XPS spectra (v) control experiments (vi) XRD, TEM and STEM EDS for aliquots.